Triple-Cation Perovskite Photoanodes for Solar Water Splitting: From Photovoltaic-Assisted to Immersed Photoelectrochemical Operation

Vera La Ferrara *, Marco Martino, Antonio Marino, Giovanni Landi, Silvano Del Gobbo, Nicola Lisi, Rosanna Viscardi, Alberto Giaconia, Giulia Monteleone

Posted Date: 5 March 2026

doi: 10.20944/preprints202603.0421.v1

Keywords: perovskite photoanode; solar water splitting; hydrogen evolution; encapsulation; ABPE; mixed-halide perovskite; photoelectrochemical devices; PET–EVA

 doi:10.20944/preprints202603.0421.v1

Article

Triple-Cation Perovskite Photoanodes for Solar Water Splitting: From Photovoltaic-Assisted to Immersed Photoelectrochemical Operation

Vera La Ferrara [1,*], Marco Martino [1], Antonio Marino [1], Giovanni Landi [2], Silvano Del Gobbo [3], Nicola Lisi [3], Rosanna Viscardi [3], Alberto Giaconia [3] and Giulia Monteleone [3]

[1] Energy Technologies and Renewable Sources Department, ENEA Portici Research Center, Portici, (Italy)
[2] Energy Efficiency Unit Department, ENEA Portici Research Center, Portici (Italy)
[3] Energy Technologies and Renewable Sources Department, ENEA Casaccia Research Center, Rome, (Italy)
* Correspondence: vera.laferrara@enea.it

Abstract

Mixed-halide perovskite solar cells with the composition $Cs_{0.1}(MA_{0.17}FA_{0.83})_{0.9}Pb(I_{0.83}Br_{0.17})_3$ were fabricated obtaining solar cells as glass/ITO/SnO_2/triple cation perovskite/HTL/Au, subsequently used as photoanodes for efficient solar-driven water splitting by applying commercial catalytic nickel foils onto the Au back-contact pads of devices. To enable operation under alkaline media the devices were encapsulated using commercial PET–EVA multilayer films, providing a robust barrier while leaving the Ni foils exposed as the electrochemically active interface. Two operating configurations were investigated and compared: (i) an outside configuration, where the perovskite solar cell powered an external electrochemical cell, and (ii) an immersed configuration, in which the encapsulated device was directly integrated into the electrolyte. In particular, the oxygen evolution reaction onset shifted from ~1.32 V vs RHE, when the Ni electrode was not powered by the perovskite absorber, to ~0.34 V vs RHE when the perovskite device powered the nickel foil for both immersed and outside configurations. The IS device achieved a maximum Applied Bias Photon-to-Current Efficiency of ~20% under AM 1.5G illumination (100 mW cm^{-2}), among the highest reported for perovskite-based photoanodes.

Keywords: perovskite photoanode; solar water splitting; hydrogen evolution; encapsulation; ABPE; mixed-halide perovskite; photoelectrochemical devices; PET–EVA

1. Introduction

Organic–inorganic hybrid perovskite solar cells (PSCs) have attracted remarkable attention as next-generation photovoltaic materials due to their high-power conversion efficiencies, low-cost fabrication, and tunable optoelectronic properties [1–3]. Despite these advantages, most perovskite devices suffer from rapid degradation upon exposure to moisture, oxygen, and light, which severely limits their operational stability and long-term performance [4]. This challenge underscores the need for innovative encapsulation strategies and device architecture that can simultaneously ensure high efficiency and environmental robustness. These intrinsic vulnerabilities remain one of the main obstacles to the commercialization of perovskite-based technologies. To enhance device durability, several strategies have been proposed, including compositional engineering, interface passivation, and the use of flexible polymeric encapsulants [5–9]. Polymeric barriers improve resistance to humidity and oxygen while enabling lightweight, robust, and portable devices compared to heavier commercial alternatives. These encapsulation approaches allow perovskite-based systems to operate in conditions unsuitable for unprotected devices [10]. Encapsulation also enables the integration of PSCs with photoelectrochemical (PEC) systems for solar driven water splitting, where protection from aqueous environment is essential. Such integrated configurations allow hydrogen production

 doi:10.20944/preprints202603.0421.v1

directly from sunlight while avoiding both the intrinsic instability of perovskites in liquid electrolytes and the need for an external power supply. Integrating the light absorber and catalytic electrodes within a compact architecture simplifies the device design, reduces energy losses, and potentially improves conversion efficiency. Moreover, the bandgap tunability of hybrid perovskites, combined with their high absorption coefficients, makes them promising photoanode materials capable of driving the oxygen evolution reaction (OER) efficiently under alkaline conditions [11–15].

The use of perovskite materials as photoanodes has gained increasing importance due to their unique combination of optoelectronic and structural properties that can overcome the limitations of conventional metal oxides. Traditional metal oxides-based photoanodes such as $BiVO_4$, WO_3, and Fe_2O_3 exhibit high stability but suffer from wide bandgaps and sluggish charge transport; however, if perovskite–$BiVO_4$ tandem architectures are realized, they can achieve unassisted water splitting with efficiencies above 6% under AM 1.5G illumination due to halide perovskites that exhibit high absorption coefficients, long carrier diffusion lengths, and adjustable bandgaps (1.5–2.2 eV) within the optimal range for solar water splitting [11]. Recent studies have demonstrated that perovskite-based photoanodes can achieve outstanding photoelectrocatalytic activity when properly protected and integrated with efficient catalysts. For instance, Hansora et al. [12] reported $FAPbI_3$/NiFeOOH photoanode with Applied Bias Photon-to-Current Efficiency (ABPE) of 7.9%. Similarly, Yang et al. [13] demonstrated that perovskite with carbon/graphite conductive protection layers and NiFe catalyst can achieve unassisted water splitting with a high ABPE of 8.5%. Recently, Fehr et al [14] confirmed the scalability of triple cation perovskite PEC systems, achieving a co-planar photocathode-photoanode architecture (Pt and IrOx catalyst for photocathode and photoanode, respectively), achieving a solar to hydrogen (STH) efficiency of 13.4% and up to 20.8% using a monolithic stacked silicon-perovskite tandem, supposing 100% faradaic efficiency. More recently, Song et al. [15] demonstrated all-perovskite tandem photocathodes capable of unassisted solar water splitting with STH efficiencies up to 15% and operational stability exceeding 120 hours under continuous illumination, confirming the viability of perovskite-based PEC systems for scalable hydrogen generation. These advances highlight the capability of perovskite materials to deliver high photovoltage (>2.0 V) and photogenerated current densities (>12 mA cm^{-2}) unbiased, while maintaining low fabrication costs and tunable optoelectronic properties. However, their integration into aqueous PEC environments remains challenging. Direct exposure to electrolytes often results in structural degradation and performance loss due to ion migration and dissolution of the perovskite layer. Hence, the development of encapsulation approaches that combine environmental stability with efficient electronic contact to catalytic electrodes is critical for advancing this technology.

Although triple-cation perovskites have been explored for their enhanced stability and electronic properties in photovoltaic architectures, their implementation as active photoanodes remains scarcely investigated. To date, the only related study is by Fehr et al. [14], which demonstrated their feasibility for water splitting but did not include a detailed PEC characterization. This work represents the second report on triple-cation perovskites for PEC applications and fills this gap by providing a complete electrochemical assessment (as for example CV, onset, photocurrent behavior and ABPE) under alkaline conditions.

In our work, we employ a triple-cation mixed-halide perovskite, $Cs_{0.1}(MA_{0.17}FA_{0.83})_{0.9}Pb(I_{0.83}Br_{0.17})_3$, as light absorber layer in n-i-p solar cells, glass/ITO/SnO_2/triple cation perovskite/HTL/Au and subsequently adapted to operate as photoanodes. This formulation of triple cation perovskite, with a higher cesium content and optimized halide ratio, enhances structural stability and interfacial charge transfer [16]. To enable operation in alkaline electrolyte, the devices were encapsulated using commercially available PET–EVA multilayer films, which provide an effective moisture barrier while allowing reliable electrical connection to Ni contacts with Au. The final architecture was glass/ITO/SnO_2/triple cation perovskite/HTL/Au/Ni. Furthermore, to the best of our knowledge, this is the first study to directly compare the performance of perovskite devices operated in two distinct configurations: (i) an outside (OS) configuration, where the perovskite cell powers an external electrochemical cell equipped with standard electrodes (Ni as working electrode

 doi:10.20944/preprints202603.0421.v1

and Pt as counter electrode), and (ii) an immersed (IS) configuration , where the encapsulated device is directly integrated into the electrolyte, where the exposed Ni foil electrode was in contact with Au metal of PSC and Pt, always, as the counter electrode. This comparison reveals how IS configuration fundamentally enhances PEC performance.

 doi:10.20944/preprints202603.0421.v1

2. Materials and Methods

2.1. Materials

SnO_2 colloid precursor (tin (IV) oxide 15% H_2O colloidal dispersion), PbI_2 (≥99.999%, ultradry), and $PbBr_2$ (Puratronic, ≥99.998%) were obtained from Alfa Aesar. CsI (≥99.999%, anhydrous) and acetonitrile (ACN) were obtained from Acros Organics. Anisole (≥99.7% anhydrous) was purchased from Sigma Aldrich. N,N-dimethylformamide (DMF), dimethyl sulfoxide (DMSO), formamidinium iodide (FAI), methylammonium bromide (MABr, ≥99%, anhydrous), Spiro-OMeTAD, chlorobenzene (CB), 4-tert-butylpyridine (TBPy), bis(trifluoromethane)sulfonimide lithium salt (Li-TFSI), and FK209 Co (III) TFSI salt were purchased from Merck. All chemicals were used without further purification. Glass/ITO substrates (2 × 2 cm^2, 10 Ω sq^{-1}, Kintec) were used as conductive supports.

2.2. Preparation of Precursors

The SnO_2 solution was prepared by diluting the commercial SnO_2 colloidal dispersion with deionized water (1:5). The perovskite precursor solution $Cs_{0.1}(MA_{0.17}FA_{0.83})_{0.9}Pb(I_{0.83}Br_{0.17})_3$ was obtained by mixing PbI_2 (1.10 M), $PbBr_2$ (0.22 M), FAI (1.05 M), and MABr (0.20 M) in DMF/DMSO (4:1 v/v). A 1.50 M CsI solution in DMSO was added to achieve 10 mol% Cs content. The hole-transport material (HTM) solution consisted of 73 mg Spiro-OMeTAD in 1 mL CB, 27 µL TBPy, 17 µL Li-TFSI solution (520 mg Li-TFSI in 1 mL ACN), and 7 µL FK209 Co (III) TFSI solution (375 mg in 1 mL ACN). The alkaline electrolyte (1 M KOH) was prepared by dissolving 5.61 g KOH pellets (≥99.99%, Merck) in 100 mL deionized water with stirring, cooled to room temperature, and freshly used.

2.3. Perovskite Based Solar Cell and Photoanode Fabrication

ITO substrates were sequentially sonicated in acetone and 2-propanol for 15 min each, dried with nitrogen, and treated under UV–ozone for 20 min. SnO_2 electron transport layers (ETL) were spin-coated at 6000 rpm for 30 s and annealed at 130 °C for 1 h. The substrates were then transferred into a nitrogen glovebox for perovskite and hole transport layer (HTL) deposition. The perovskite layer was spin-coated using a two-step program (1000 rpm for 10 s and 6000 rpm for 20 s), with 200 µL anisole was added dropwise as an antisolvent. Films were annealed at 100 °C for 1 h. The Spiro-OMeTAD layer, as HTL, was spin-coated at 4000 rpm for 30 s, followed by thermal evaporation of 80 nm Au back contact [16]. To use the pristine perovskite solar cell as a photoanode for PEC testing, the device was modified by adding two nickel foils onto its existing electrical contacts, one on the Au pad and one on the ITO coated glass substrate, named Ni (+) and Ni (-) respectively (Figure 1a). Given the higher rigidity and hardness of nickel compared to gold, small drops of silver conductive paste were applied between the Au pads (or ITO) and the Ni foils to improve electrical contact. To evaluate a suitable thickness of nickel foils for photoelectrocatalytic integration, the current density–voltage (J–V) characteristics of pristine perovskite devices were first recorded under standard illumination (AM 1.5G, 100 mW cm^{-2}) and compared with PSCs with nickel foils of varying thicknesses as the electrode. Among the thicknesses, 20 µm-thick nickel foil exhibited the best performance. The perovskite devices were then encapsulated using multilayer polymeric film lamination between two PET–EVA sheets and laminated under mild heat and pressure to form an effective moisture barrier, at 100 °C and 0.5 MPa for 5 min. The PET layer provided mechanical stability and optical transparency, whereas the EVA layer ensured strong adhesion and air and watertight sealing. A Kapton polyimide tape was first applied to protect the active area from direct exposure to the encapsulant. Front and back-view images of the encapsulated devices are shown (Figure 1b).

 doi:10.20944/preprints202603.0421.v1

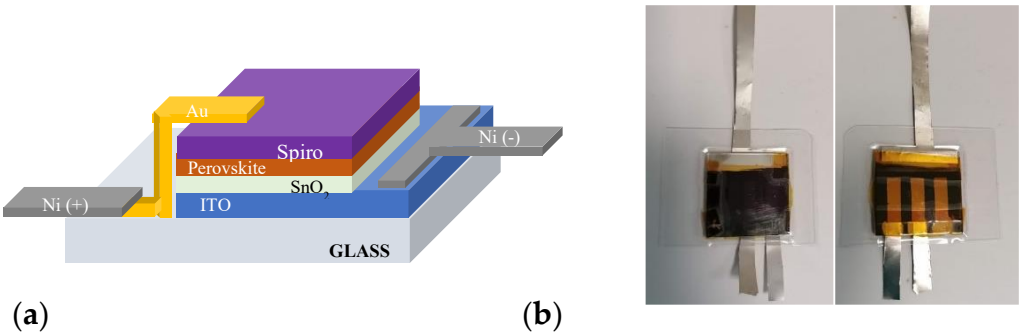

(a) (b)

Figure 1. (**a**) Schematic representation of the n-i-p perovskite solar cell architecture (Glass/ITO/SnO_2/Perovskite/Spiro-OMeTAD/Au) showing the placement of nickel electrodes in contact with Au and ITO terminals of the device. (**b**) Photographs of the typical perovskite device encapsulated using multilayer polymeric films (PET–EVA). (left), front, where glass is illuminated by solar simulator, and (right) back, where Nickel foils are deposited on Au pads and on ITO.

3. Results and discussion

3.1. Perovskite-based PEC Configurations and characterization of Standard Electrochemical Cell

The photoelectrochemical performance of the encapsulated PSCs was evaluated in two operational configurations: (i) outside (OS) configuration, where the perovskite cell powered an external standard electrochemical cell, and (ii) immersed (IS) one, where the encapsulated device was directly integrated into the electrolyte, using the Ni foil in contact with the Au terminal as the working electrode. Illumination was provided by a LED AM 1.5G solar simulator (OSSILA, 100 mW cm^{-2}) (Figure 2). The standard electrochemical had three-electrode configuration with 1 M KOH electrolyte, with Ni as the working electrode, Pt as the counter electrode, and Ag/AgCl as reference (Figure. 3). The nickel electrode drove the oxygen evolution reaction (OER) at the anode ($4OH^- \rightarrow O_2 + 2H_2O + 4e^-$), while the platinum counter electrode catalyzed the hydrogen evolution reaction (HER) at the cathode ($4H_2O + 4e^- \rightarrow 2H_2 + 4OH^-$). The overall process corresponded to water splitting ($2H_2O \rightarrow 2H_2 + O_2$). The cyclic voltammetry (CV) recorded on the Ni/Pt electrodes, biased with a potentiostat, but in the absence of the perovskite solar cell (i.e., without any photovoltage contribution) shows the characteristic behavior of alkaline OER, with an anodic onset potential appearing at approximately $E_{(onset\ (vs.\ Ag/AgCl))} = +0.30$ V vs Ag/AgCl. The onset potential (E_{onset}) is conventionally defined as the potential at which the photocurrent density reaches a small but measurable value (typically 0.0001–0.0002 A cm^{-2} above the baseline), and represents the minimum external bias required to initiate the electrochemical reaction.

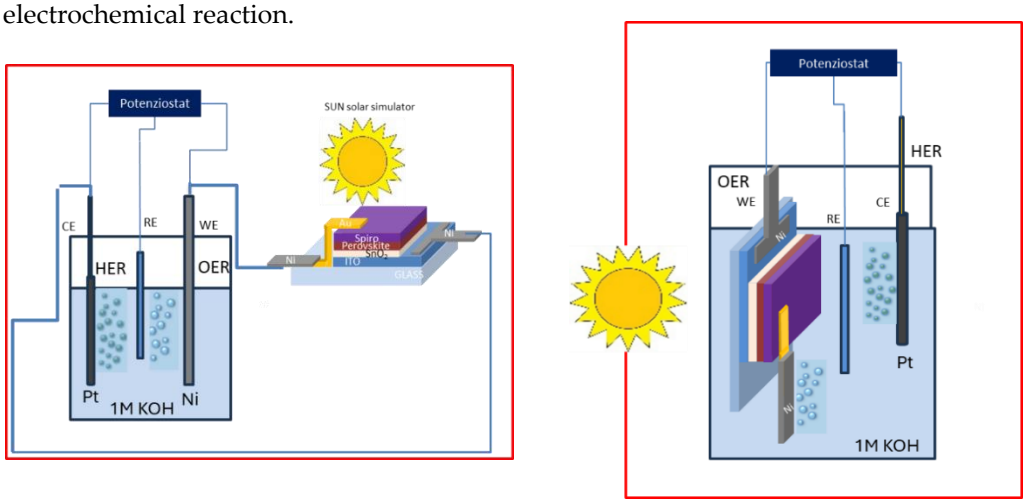

(a) (b)

 doi:10.20944/preprints202603.0421.v1

Figure 2. Schematic representation of the encapsulated PSC in (**a**) outside and (**b**) immersed configuration with Nickel as the working electrode and platinum as the counter electrode and the third electrode as reference.

Figure 3. Standard photoelectrochemical cell used for water-splitting experiments in 1 M KOH aqueous electrolyte. The electrodes are biased to the potentiostat via alligator clips.

To demonstrate the analyzed results, the measured potentials are converted into potential versus reversible hydrogen electrode (RHE) using [17]:

$$E_{RHE} = E_{Ag/AgCl} + E^{0}_{Ag/AgCl} + 0.059 \times pH \quad (1)$$

The potential of the reference electrode, concerning the standard hydrogen electrode at 25 °C (0.197 V for Ag/AgCl), is denoted as $E^{0}_{Ag/AgCl,}$ while the working potential measured versus the reference electrode is represented as $E_{Ag/AgCl}$. Thus, the OER onset corresponds to approximately 1.32 V vs RHE for nickel-based catalysts in alkaline media (1 M KOH, pH=14) (Figure 4). The $Ni(OH)_2$/NiOOH redox transition, which reflects the formation of active NiOOH sites, occurs at a lower potential of around 1.1 V vs RHE.

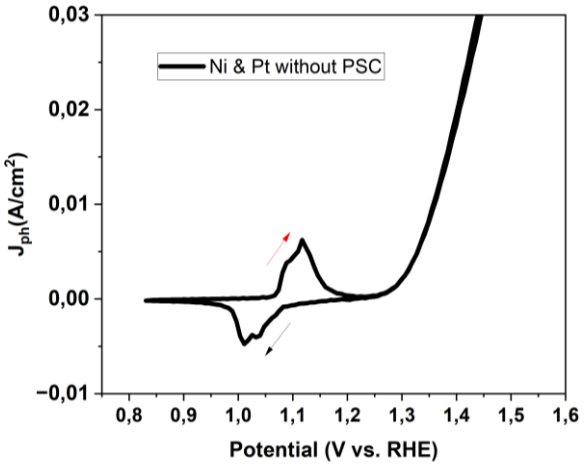

Figure 4. Cyclic voltammetry curve of a standard electrochemical cell, biased with a potentiostat, employing nickel as the working electrode and platinum as the counter electrode in 1 M KOH aqueous solution, at scan rate 100 mV/s. The arrows indicate the direction: from positive to negative voltages (dark arrow, reduction) and from negative to positive voltages (red arrow, oxidation).

3.2. Encapsulated device characterization for PEC applications

After fabrication of PSCs, the J–V characteristics under LED solar simulator, recorded before and after encapsulation are shown in Figure 5. The nearly overlapping curves confirm that the encapsulation processes do not affect the electrical performance of the devices. To assess whether the encapsulation procedure alters the photovoltaic performance of the devices, a statistical comparison of the key photovoltaic (PV) parameters (short circuit current density, Jsc, open circuit voltage, Voc, fill factor, FF, and power conversion efficiency, PCE) was carried out before and after encapsulation.

 doi:10.20944/preprints202603.0421.v1

Figure 6 shows the distribution of each parameter across multiple devices, represented as box-and-whisker plots with the individual datapoints overlaid. This analysis allows a direct evaluation of potential degradation or variability induced by the encapsulation process. The distributions of PV parameters reveal that encapsulation does not negatively affect the PV performance of the PSCs. A slight increase in Jsc is observed after encapsulation, which may be attributed to reduced surface recombination or improved optical confinement induced by the encapsulation layer. These results validate the robustness of the encapsulation strategy and demonstrate that devices maintain full photovoltaic functionality before being implemented as photoanodes in PEC measurements.

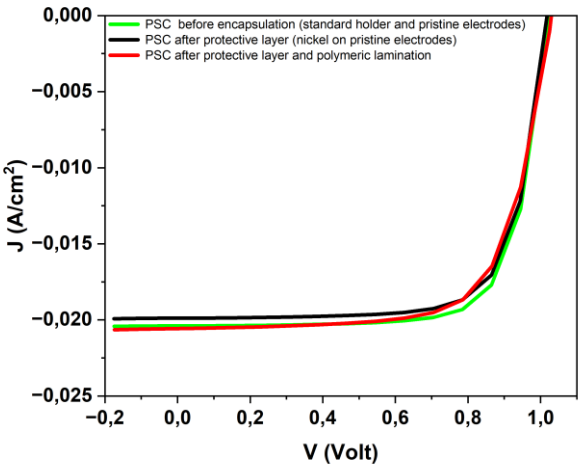

Figure 5. Typical J–V characteristics of PSCs recorded before and after encapsulation. The green curve corresponds to the pristine device measured in the standard holder with original electrodes (gold as positive and ITO as negative electrode); the black curve represents the device after applying the protective Kapton layer and catalytic nickel foil electrodes on the pristine contacts; and the red curve shows the device after full encapsulation with the polymeric multilayer lamination (PET–EVA).

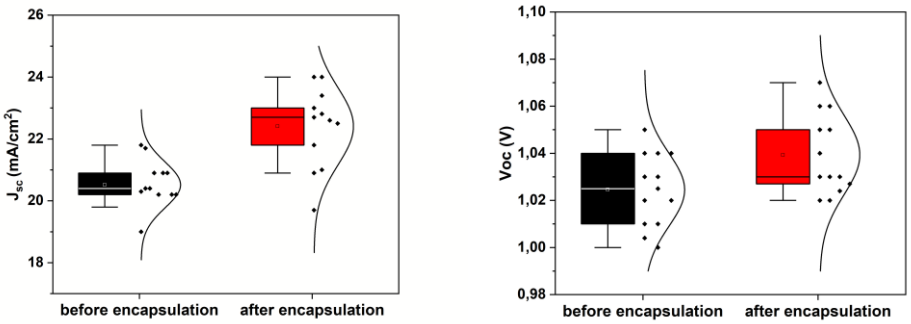

(**a**) (**b**)

Preprints.org (www.preprints.org) | NOT PEER-REVIEWED | Posted: 5 March 2026 doi:10.20944/preprints202603.0421.v1

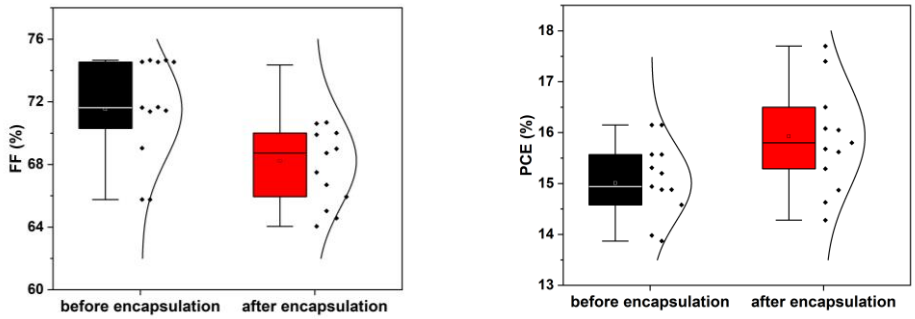

(**c**) (**d**)

Figure 6. Statistical distribution of photovoltaic parameters before and after encapsulation: (**a**) short-circuit current density (J_{sc}), (**b**) open-circuit voltage (V_{oc}), (**c**) fill factor (FF) and (**d**) power conversion efficiency (PCE).

3.3. Experimental Setup for Perovskite Solar Cells in outside and immersed Configurations

The photoelectrochemical performance of the encapsulated PSCs (called PSC A, PSC B, PSC C and PSC D) was evaluated in two operational configurations: outside and immersed.

3.3.1. Outside configuration

In the OS configuration, the encapsulated PSCs operated as independent light-harvesting units, directly powering the external electrochemical cell for water splitting. Figure 7 shows the corresponding photographs. The left panel displays the full experimental setup, including the electrochemical cell, the solar simulator, and the microprobes used to contact the external perovskite solar cell. In the central image, a single external PSC is contacted with two microprobes, while the right image shows two PSCs connected in series and contacted in the same manner, both illuminated under identical conditions.

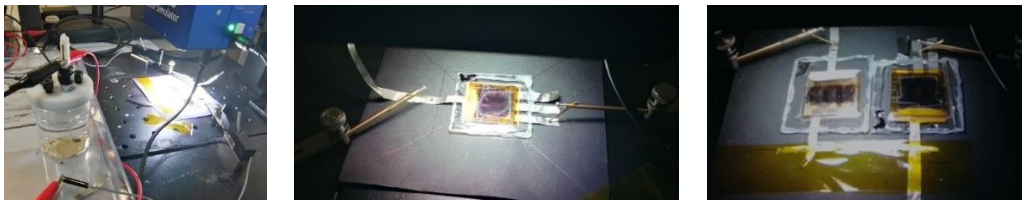

Figure 7. Photographs of the experimental setup used for testing PSCs in outside configuration under LED solar illumination. (Left) The encapsulated PSC is connected externally to the standard electrochemical cell (Center) Single perovskite solar cell, (Right) Two PSCs connected in series.

A typical J–V curves (Figure 8) confirm that connecting two PSCs in series increases the open-circuit voltage (V_{oc}) as expected, while the current density (J) decreases slightly due to additional contact resistance introduced by the series connection. In the OS configuration, the only driving force for the reaction was the photovoltage delivered by the perovskite solar cell placed outside the electrolyte, which powered the Ni/Pt electrochemical cell. All measurements in alkaline electrolyte were performed under zero applied bias from the potentiostat. No hydrogen evolution was detected in the dark, confirming the absence of spontaneous electrochemical activity. Under illumination, the photocurrent was observed, demonstrating that the photovoltage generated by external PSCs was sufficient to autonomously power the water-splitting reaction. The chronoamperometric response (Figure 9) clearly shows a marked increase in photocurrent (J_{ph}) upon illumination, corresponding to hydrogen generation, and a return to baseline in the dark.

 doi:10.20944/preprints202603.0421.v1

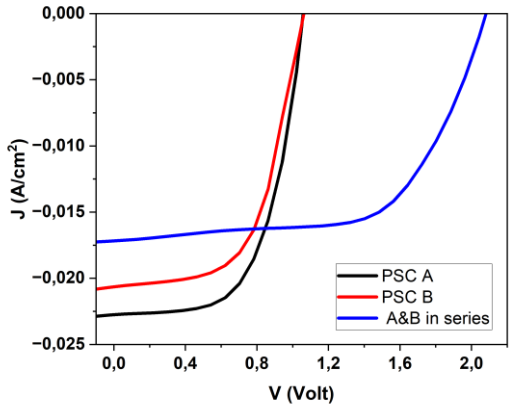

Figure 8. Typical current density–voltage (J–V) characteristics of one PSC and of the two devices connected in series, lighted with LED solar simulator.

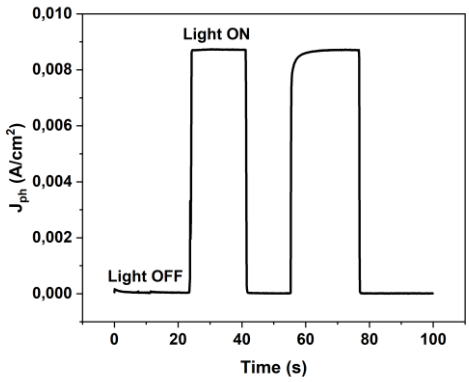

Figure 9. Photocurrent density of the photoelectrochemical cell connected to PSCs in series, lighted by LED solar simulator and no bias with potentiostat.

3.3.2. Immersed Configuration

In the IS configuration, the encapsulated perovskite solar cell was directly placed in the alkaline electrolyte, serving simultaneously as the photovoltaic absorber and as the mechanical support for the nickel electrode that defined the active area, and no bias is applied from the potentiostat. In this arrangement, the PSC was fully integrated within the electrochemical environment. Photographs of the experimental setup are presented in Figures 10 and 11, where LED solar simulator lighted through the substrate glass side. The light beam was oriented perpendicularly to the photoanode surface to ensure uniform illumination of the active area. Figure 12 compares the transient photocurrent generated (J_{ph}) by one PSC when contacted with either one or two nickel foils. When two Ni foils are connected to the two Au pads of the PSC (red curve), the photocurrent nearly doubles relative to the configuration with a single Ni foil (black curve). This increase is consistent with the increasing of the electrochemically active area while the operating voltage remains unchanged, confirming that the photocurrent scales proportionally with the area of active Ni contact interfaces participating in the OER process. The transient J_{ph}–t profiles exhibited clear ON/OFF photoresponses synchronized with light modulation, confirming that no reaction occurred in the dark and unbiased (see Video S1 and S2 recorded with a single nickel foil and two nickel foils, respectively).

 doi:10.20944/preprints202603.0421.v1

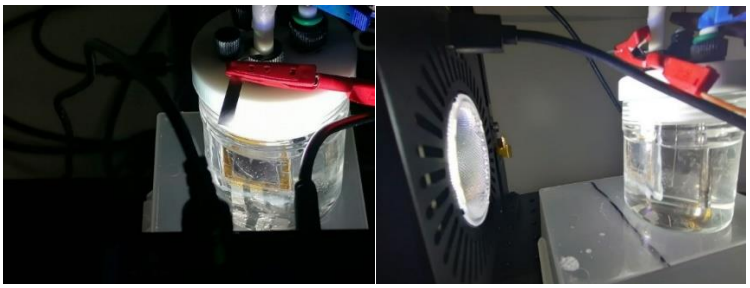

Figure 10. Photographs of the photoelectrochemical setup when perovskite-based photoanode was immersed. (Left) The encapsulated perovskite-based photoanode illuminated through the glass substrate using the LED solar simulator. (Right) another view of the same setup during operation.

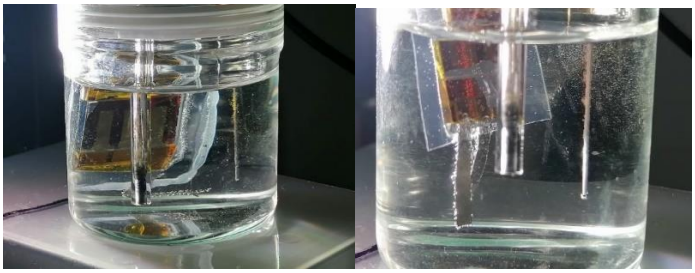

Figure 11. Magnified views of the perovskite-based photoanode showing the actual placement of the nickel electrodes on the Au terminals after encapsulation. (a) Configuration with a single Ni electrode placed on one Au pad of the device (b) Configuration with two Ni electrodes positioned on two separate Au pads, defining independent photoactive areas sharing a common ITO contact.

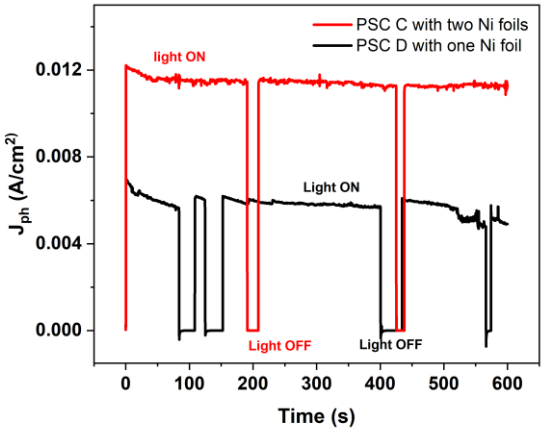

Figure 12. Photocurrent–time (J_{ph}–t) response of photoanode under illumination but no bias with potentiostat. The black curve corresponds to a device with a single Ni foil electrode placed on one Au pad, while the red curve refers to device with two Ni foils electrodes positioned on two separate Au pads. PSC C- Ni foil 0.56 cm^2 each, PSC D – Ni foil 0.6 cm^2

The influence of externally applied bias from the potentiostat on the PEC performance was also examined (Figure 13). As expected, the photocurrent increased if 300 mV bias was applied, indicating improved charge separation and enhanced interfacial charge-transfer kinetics. No measurable current or hydrogen evolution was observed in the dark, even under applied bias, confirming the strictly photoinduced nature of the process.

 doi:10.20944/preprints202603.0421.v1

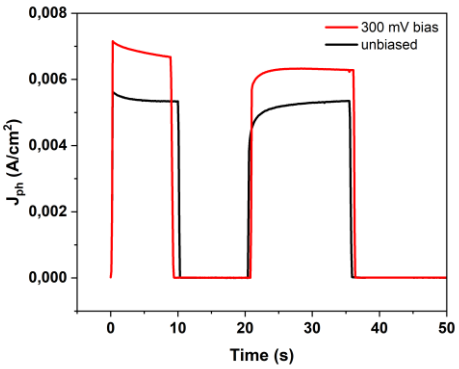

Figure 13. Photocurrent–time response of the immersed perovskite photoanode under chopped illumination. The black curve corresponds to measurements performed at 0 V bias, while the red curve represents data acquired under an applied bias of +300 mV. PSC had 3 Nickel foils, 0.5 cm² each.

3.4. Photoelectrochemical Response: Outside vs. Immersed Configuration

A comparative CV analysis was performed on the same encapsulated PSC, first operated outside the electrolyte and then immersed in the electrolyte to enable a direct comparison. The measurements were also compared with those of a standard Ni electrode measured without the perovskite solar cell. (Figure 14). The CV curves were recorded without iR compensation; however, the series resistance of the system (4–7 Ω) results in a negligible uncompensated drop, making this correction unnecessary for interpreting the data. Both configurations, OS and IS, exhibit hysteresis between the reduction and oxidation scans, a characteristic of perovskite-based photoelectrodes associated with ionic migration and capacitive charging within the halide perovskite absorber [18]. However, hysteresis is noticeably more pronounced in the OS configuration (dark curve figure 14), indicating slower interfacial equilibration and higher recombination losses when the device is electrically connected through external wiring. In contrast, the immersed device shows a more stable and reproducible CV shape, suggesting improved charge-transfer kinetics. These slow interfacial and bulk relaxation processes produce a history-dependent electrochemical response, not present in the standard electrochemical cell when nickel and platinum electrodes were not powered by the perovskite solar cell (blue curve figure 14). Moreover, in the IS configuration (red curve figure 14), the photocurrent increases more rapidly and reaches higher values compared to the OS configuration. The onset potential for oxygen evolution shifts dramatically when the PSC is used for powering the nickel foil electrode for both IS and OS configurations. While the Ni/Pt electrochemical cell, not powered by the perovskite absorber, exhibits an onset around 1.32 V vs RHE (Figure 14 blue curve), both the IS and OS PSC–Ni configurations show a much earlier onset at ~0.34 V vs RHE (Figure 14 black and red curves).

 doi:10.20944/preprints202603.0421.v1

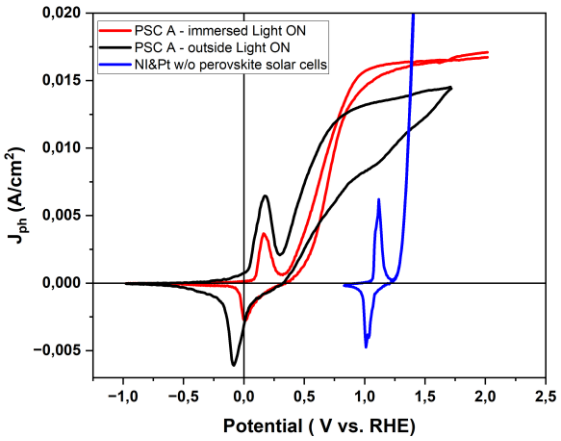

Figure 14. Cyclic voltammetry curves of the encapsulated perovskite in both OS and IS configurations, dark and red curves respectively, compared to the cyclic voltammetry of a standard electrochemical cell (the blue one).

This strong reduction in overpotential does not originate from the Ni–electrolyte interface itself, as nickel already forms $Ni(OH)_2$/NiOOH in the standard cell, but rather from the photovoltage and photogenerated holes supplied by the perovskite absorber directly into the NiOOH catalytic sites, triggering the $Ni(OH)_2$/NiOOH redox transition at approximately 177 mV (Figure 14 black and red curves). This value is markedly lower than the anodic peak observed at ~1.1 V in the configuration where the electrochemical cell operates without being powered by the PSC (Figure 14 blue curve). This comparison clearly shows that the photovoltage provided by the perovskite significantly lowers the energetic threshold required for Ni activation in alkaline media. Furthermore, the IS configuration shows the highest photocurrents and the most favorable kinetics, whereas the OS configuration still benefits from photovoltage assistance but is limited by additional resistive and interfacial losses. Overall, the comparison demonstrates that the perovskite solar cell is responsible for the drastic reduction in OER onset potential and that direct immersion maximizes the efficiency of photovoltage transfer to the catalytic interface and reduces hysteresis compared to the OS configuration. Although the CV curves highlight clear differences in onset potential and photocurrent behavior between the two configurations, a quantitative metric is needed to determine how effectively the devices convert absorbed photons into chemical output. Future work will include direct H_2/O_2 quantification (Solar-to-Hydrogen (STH) efficiency) and Faradaic efficiency measurements to validate the energy conversion. Direct quantification of H_2/O_2 and Faradaic efficiency was beyond the scope of this study but will be essential for validating practical energy conversion in future work. Meanwhile, in this study, we calculated the Applied Bias Photon-to-Current Efficiency (ABPE), which offers a direct and reliable measure of photoelectrochemical performance.

The ABPE is defined as:

$$ABPE\ (\%) = \frac{Jph * (1.23 - Vbias)}{Pin} \times 100 \quad (2)$$

where J_{ph} is the photocurrent density (A cm^{-2}), 1.23 V is the thermodynamic potential required for water splitting, V_{bias} is the applied bias potential, and P_{in} is the incident light power density (100 mW cm^{-2} under standard AM 1.5G solar illumination). The potential corresponding to the maximum of the ABPE curve is referred to as the optimal bias (V_{opt}), which represents the point of maximum conversion efficiency (Figure 15).

 doi:10.20944/preprints202603.0421.v1

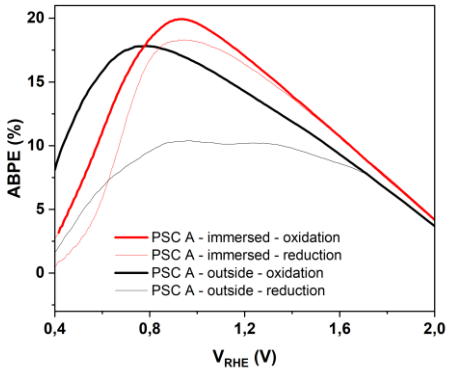

Figure 15. Applied Bias Photon-to-Current Efficiency curves for the PSC operated in the OS and IS configurations.

The IS configuration delivers the highest ABPE (~19.9%) because it minimizes contact resistance and enables more efficient photovoltage transfer to the Ni/NiOOH interface, whereas the OS configuration (~17.8%) remains limited by additional wiring and interfacial losses. Table I summarizes the photoelectrochemical parameters obtained for both the IS and OS configurations.

Table I. Summary of key photoelectrochemical parameters for the PSC operated in the OS and IS configurations

Configuration	V_{Onset} (V vs. RHE)	V_{opt} (V vs. RHE)	Jph (mA/cm²)	$ABPE_{max}$ (%)
IS (oxidation curve)	0.34	0.93	15.7	~19,93
IS (reduction curve)	0.34	0.93	15.7	~18,31
OS (oxidation curve)	0.34	0.75	13.6	~17.80
OS (reduction curve)	0.34	0.93	9.9	~10.39

To examine the effective operating conditions of the device in different configurations, the J–V curve, measured for pristine PSC in photovoltaic (PV) mode (before immersion), was overlaid with the photocurrent–potential characteristics extracted from cyclic voltammetry in the IS and OS configurations (Figure 16). This combined representation directly shows how much of the photovoltage generated by the perovskite can be transferred to the electrochemical reaction under each operating mode.

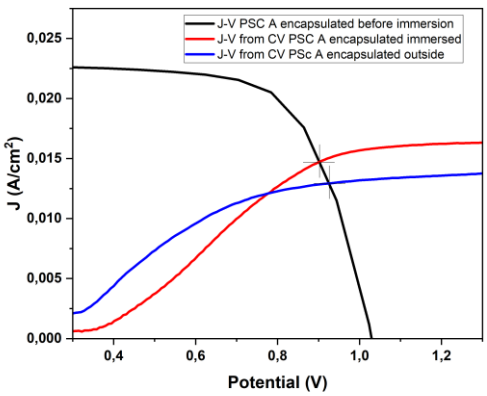

 doi:10.20944/preprints202603.0421.v1

Figure 16. J–V curve of the perovskite solar cell (black, before immersion) overlaid with the photocurrent–potential responses extracted from CV in the IS (red) and OS (blue) configurations. The intersection point indicates the self-driven operating condition for OER without external bias.

In PV mode (black curve), the device shows V_{oc} of ~1.05 V and short-circuit current density exceeding 20 mA cm^{-2}, representing the maximum power available from the perovskite absorber. When the same device operates as an immersed photoanode (red curve), the anodic photocurrent follows a markedly different J–V trajectory, intersecting the PV curve at approximately 0.89 V and ~14.7 mA cm^{-2}. This intersection defines the potential operating point at which the photovoltage generated by the perovskite is sufficient to sustain OER without external bias. The higher current at the intersection reflects the more efficient transfer of photovoltage to the Ni/NiOOH interface in the IS configuration, in accordance with improved charge-transfer kinetics and reduced interfacial losses. In contrast, the OS configuration (blue curve) exhibits lower photocurrent and its intersection with the PV curve occurs at a much smaller current density and at a higher voltage, 0.93V, closer to Voc. This indicates that only a limited fraction of the available photovoltage is effectively transferred to the electrochemical cell when the device is not immersed, due to additional series resistance and wiring losses, and the absence of direct semiconductor–electrolyte coupling. As a result, the OS configuration operates close to the OER onset, which explains why only a few high-performing cells can drive oxygen evolution in this configuration

3.5. Stability of Immersed Device

To evaluate the operational long-term stability of the immersed perovskite-based photoanode, an aging test was carried out under continuous illumination with a LED solar simulator in 1 M KOH, with simultaneous monitoring of the photocurrent and visual inspection of the device over time (Figure 17).

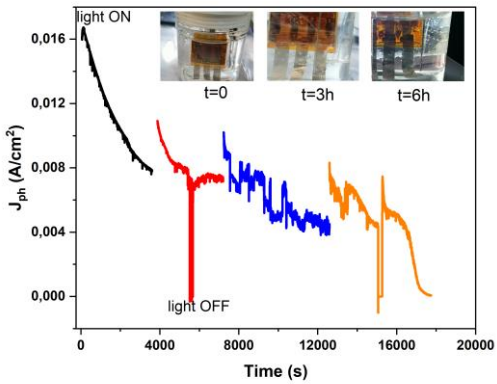

Figure 17. Photocurrent stability of the immersed perovskite-based photoanode under continuous illumination in 1 M KOH, together with photographs of the device at t = 0 h, 3 h, and 6 h during immersion.

At t = 0 h, the photograph (inset of figure 17) shows the device at the beginning of the immersion). After ~3 h of immersion, a yellowish coloration becomes visible along the edges of the encapsulation, indicating that although the PET–EVA lamination provides a good barrier against moisture and alkaline exposure, it is insufficient on its own to fully protect the device edges from electrolyte penetration. Additionally, epoxy resin was applied at the borders to reinforce edge sealing, but partial penetration still occurred during prolonged operation. After 6 h, the perovskite layer shows complete degradation, accompanied by a sharp decrease in photocurrent, confirming that device failure occurs once the electrolyte reaches the active layer. The observed edge degradation likely originates from electrolyte penetration through imperfect sealing, leading to perovskite dissolution and ion migration. Future work should explore advanced edge-sealing materials or multi-

 doi:10.20944/preprints202603.0421.v1

layer encapsulation strategies. Previous studies have shown that PET–EVA encapsulation can offer effective environmental protection in alkaline media [19,20], suggesting that the operational stability observed here could be further extended through improved edge-sealing strategies.

3.6. Comparison with Literature-Reported Approaches

Table II compares the IS configuration presented in this study with previously reported approaches in the literature.

As highlighted in Table II, the device presented here delivers the highest ABPE reported to date for a perovskite photoanode, outperforming previously published systems across efficiency-related metrics. In terms of stability, our triple-cation perovskite shows a degradation timescale (~5 h) like the only comparable triple-cation system in the literature [15], whereas single-cation perovskites tend to remain stable for longer but at the cost of substantially lower performance. The ABPE achieved in our work (~20%) represents a significant improvement compared to previous reports (≤8.5%), confirming the potential of triple-cation perovskites for high-efficiency PEC systems.

Table 2. M KOH, illumination 100mW **cm⁻².**

Photoelectrode configuration	Jph (mA/cm²) at 1.23 V vs. RHE	ABPE (%)	STH (%)	Aging	Ref.
$Cs_{0.1}(MA_{0.17}FA_{0.83})_{0.9}Pb(I_{0.83}Br_{0.17})_3$ immersed photoanode/Nickel foil	16.4	19.9		5 h	**This work**
$MAPbI_3$ –$BiVO_4$ photoanode tandem –outside PSC	5.01	6.2			[11]
$FAPbI_3$/Ni/ NiFeOOH – immersed photoanode	22.8		9.8	3 days	[12]
$FAPbBr_3$/ carbon/graphite/ NiFe immersed Photoanode	9.12	8.5		100 h	[13]
$Cs_{0.05}FA_{0.85}MA_{0.1}Pb(I_{0.95}Br_{0.05})_3$ & $FA(PbI_3)_{0.97}(MAPbI_3)_{0.03}$ immersed photocathode&photoanode	20	13.4*		5 h	[14]
Tandem perovskite/silicon phoanode	16.9 10	20.8* 13.4*		1 h 102 h	

*Fehr et al. reported STH efficiencies assuming a 100% Faradaic efficiency for the catalysts, which corresponds to an ABPE.

This comparison underscores the trade-off between efficiency and durability currently observed in the field and demonstrates that high-performing perovskite photoanodes can be achieved through

 doi:10.20944/preprints202603.0421.v1

effective device design and semiconductor–electrolyte integration. Further improvements in encapsulation and edge sealing will be required to extend operational lifetimes while maintaining the high efficiency demonstrated here.

4. Conclusions

This work provides the first systematic comparison between OS and IS configurations of encapsulated mixed-halide PSCs, demonstrating that immersion markedly improves charge-transfer kinetics and, overall, PEC efficiency for solar-driven water splitting. Since the perovskite layer remains fully encapsulated, the performance enhancement does not arise from direct semiconductor–electrolyte contact, but rather from the reduced contact and wiring losses and the more effective delivery of the photovoltage to the Ni catalytic interface when the integrated device is operated directly in the electrolyte. When combined with Ni foils, the photovoltage generated by the triple-cation perovskite lowers the oxygen evolution onset potential by nearly 1 V compared to the standard Ni/Pt electrochemical cell operating without any PSC. Under AM 1.5G illumination, the IS architecture achieves a maximum ABPE of ~20%, among the highest reported for perovskite-based photoanodes. To the best of our knowledge, this is the first study to directly compare the behavior of perovskite-based PEC devices in IS and OS configurations, providing new insight into how device architecture and electrolyte operation influence photovoltage deployment and catalytic activation. The observed performance gains result from the synergistic effect of the triple-cation composition, the optimized halide ratio, robust encapsulation enabling alkaline stability, and the direct electrolyte exposure of the Ni catalytic layer. These findings highlight the decisive role of device architecture in unlocking the PEC potential of perovskite absorbers and outline a clear pathway toward high-efficiency integrated photoanodes. Future efforts should focus on advanced encapsulation and edge-sealing strategies to extend operational durability and support the practical deployment of perovskite-based solar hydrogen technologies. These findings outline a viable route toward scalable PEC architectures based on perovskite absorbers, provided that the remaining challenges related to encapsulation and long-term durability are effectively addressed.

Supplementary Materials: The following supporting information can be downloaded at: Preprints.org, Video S1: “One Nickel foil and PSC immersed”; Video S2: “Two Nickel foils and PSC immersed”;

Author Contributions: Conceptualization, V.L.F., N.L., S.D.G. and M.M.; methodology, V.L.F., N.L., S.D.G., M.M. and A.M.; validation, V.L.F., M.M., A.M., G.L., S.D.G., N.L., R.V., A.G. and G. M.; formal analysis, V.L.F., G.L., S.D.G. and R.V.; investigation, V.L.F. and A.M.; writing—original draft preparation, V.L.F..; writing—review and editing, V.L.F., M.M., G.L., S.D.G., N.L., R.V., A.G. and G.M.; project administration, A.G.; funding acquisition, G.M. All authors have read and agreed to the published version of the manuscript.

Funding: This research was funded by the European Union – NextGeneration EU from the Italian Ministry of Environment and Energy Security, POR H2 AdP MEES/ENEA with involvement of CNR and RSE, PNRR - Mission 2, Component 2, Investment 3.5 "Ricerca e sviluppo sull’idrogeno", CUP: I83C22001170006

Conflicts of Interest: The authors declare no conflicts of interest

Abbreviations

The following abbreviations are used in this manuscript:

OS	Outside
IS	Immersed
OER	Oxygen Evolution Reaction
HER	Hydrogen Evolution Reaction
ABPE	Applied Bias Photon-to-Current Efficiency
RHE	Reversible Hydrogen Electrode
PET–EVA	poly (ethylene terephthalate) - ethylene vinylacetate
AM	Air Mass
PSC	Perovskite Solar Cell

 doi:10.20944/preprints202603.0421.v1

PEC	Photoelectrochemical
STH	Solar to Hydrogen
CV	Cyclic Voltammetry
ITO	Indium tin oxide
n-i-p	negative-intrinsic-positive
ETL	Electron Transport Layer
HTL	Hole Transport Layer
J–V	Current density - voltage
LED	Light Emitting Diode
J_{sc}	Short circuit current density
V_{oc}	Open circuit voltage
FF	Fill factor
PCE	Power conversion efficiency
J_{ph}	Photocurrent density
PV	Photovoltaic
V_{opt}	Optimal bias

References

1. NREL Best Research-Cell Efficiency Chart, https://www.nrel.gov/pv/cell-efficiency.html (accessed 2026).
2. Green, M., Ho-Baillie, A., Snaith, H. The emergence of perovskite solar cells. *Nature Photon* **2014**, 8, 506–514. https://doi.org/10.1038/nphoton.2014.134
3. Park, N.-G., Zhu, K. Scalable fabrication and coating methods for perovskite solar cells and solar modules. *Nat Rev Mater* **2020**, *5*, 333–350. https://doi.org/10.1038/s41578-019-0176-2
4. Niu, G., Li, W., Li, J., Liang, X., Wang, L. Enhancement of thermal stability for perovskite solar cells through cesium doping. *RSC Adv* **2017**, *7*, 17473–17479. https://doi.org/10.1039/C6RA28501E
5. Jeong, M., Choi, I. W., Go, E. M., Cho, Y., Kim, M., Lee, B., Jeong, S., Jo, Y., Choi, H. W., Lee, J., Bae, J. H., Kwak, S. K., Kim, D. S., Yang, C. Stable perovskite solar cells with efficiency exceeding 24.8% and 0.3-V voltage loss. *Science* **2020**, *369*, 1615–1620. https://doi.org/10.1126/science.abb7167
6. Ahn, N., Son, D. Y., Jang, I. H., Kang, S. M., Choi, M., Park, N.-G. Highly reproducible perovskite solar cells with average efficiency of 18.3% and best efficiency of 19.7% fabricated via Lewis base adduct of lead(II) iodide. *J Am Chem Soc* **2015**, *137*, 8696–8699. https://doi.org/10.1021/jacs.5b04930
7. Yang, Y., Song, X., Liu, H., Zhang, A., Cao, J., Wu, C. Encapsulation-driven stability in perovskite solar cells: suppressing degradation through hermetic sealing. *ACS Appl Mater Interfaces* **2025**, *17*, 34119–34128. https://doi.org/10.1021/acsami.5c02993
8. Aitola, K., Gava Sonai, G., Markkanen, M., Kaschuk, J. J., Hou, X., Miettunen, K., Lund, P. D. Encapsulation of commercial and emerging solar cells with focus on perovskite solar cells. *Sol Energy* **2022**, *237*, 264–283. https://doi.org/10.1016/j.solener.2022.03.060
9. Dipta, S. S., Rahim, M. A., Uddin, A. Encapsulating perovskite solar cells for long-term stability and prevention of lead toxicity. *Appl Phys Rev* **2024**, *11*, 021301. https://doi.org/10.1063/5.0197154
10. Chu, Q.-Q., Sun, Z., Wang, D., Cheng, B., Wang, H., Wong, C.-P., Fang, B. Encapsulation: The path to commercialization of stable perovskite solar cells. *Matter* **2023**, *6*, 3838–3863. https://doi.org/10.1016/j.matt.2023.08.016
11. Qiu, Y., Liu, W., Chen, W., Zhou, G., Hsu, P.-C., Zhang, R., Liang, Z., Fan, S., Zhang, Y., Cui, Y. Efficient solar-driven water splitting by nanocone $BiVO_4$–perovskite tandem cells. *Sci Adv* **2016**, *2*, e1501764. https://doi.org/10.1126/sciadv.1501764
12. Hansora, D., Yoo, J. W., Mehrotra, R., Byun, W. J., Lim, D., Kim, Y. K., Noh, E., Lim, H., Jang, J. W., Seok, S. I., Lee, J. S. All-perovskite-based unassisted photoelectrochemical water splitting system for efficient, stable and scalable solar hydrogen production. *Nat Energy* **2024,** *9*, 272–284. https://doi.org/10.1038/s41560-023-01438-x
13. Yang, H., Liu, Y., Ding, Y., Li, F., Wang, L., Cai, B., Zhang, F., Liu, T., Boschloo, G., Johansson, E. M. J., Sun, L. Monolithic $FAPbBr_3$ photoanode for photoelectrochemical water oxidation with low onset-potential and enhanced stability. *Nat Commun* **2023**, *14*, 5486. https://doi.org/10.1038/s41467-023-41187-9

 doi:10.20944/preprints202603.0421.v1

14. Fehr, A. M. K., Agrawal, A., Mandani, F., Conrad, C. L., Jiang, Q., Park, S. Y., Alley, O., Li, B., Sidhik, S., Metcalf, I., Botello, C., Young, J. L., Even, J., Blancon, J.-C., Deutsch, T. G., Zhu, K., Albrecht, S., Toma, F. M., Wong, M., Mohite, A. D. Integrated halide perovskite photoelectrochemical cells with solar-driven water-splitting efficiency of 20.8%. *Nat Commun* **2023**, *14*, 3797. https://doi.org/10.1038/s41467-023-39290-y
15. Song, Z., Li, C., Chen, L., Dolia, K., Fu, S., Sun, N., Li, Y., Wyatt, K., Young, J. L., Deutsch, T. G., Yan, Y. All-perovskite tandem photoelectrodes for unassisted solar hydrogen production. *ACS Energy Lett* **2023**, *8*, 2611–2619. https://doi.org/10.1021/acsenergylett.3c00654.
16. La Ferrara, V., De Maria, A., Rametta, G. Green anisole as antisolvent in planar triple-cation perovskite solar cells with varying cesium concentrations. *Micromachines* **2024**, *15*, 136. https://doi.org/10.3390/mi15010136
17. Garcia, A. C., Koper, M. T. M. Effect of saturating the electrolyte with oxygen on the activity for the oxygen evolution reaction. *ACS Catal* **2018**, *8*, 9359–9363. https://doi.org/10.1021/acscatal.8b01447
18. Tress, W., Marinova, N., Inganäs, O., Nazeeruddin, M. K., Zakeeruddin, S. M., Grätzel, M. Understanding the rate-dependent J–V hysteresis, slow time component, and aging in $CH_3NH_3PbI_3$ perovskite solar cells. *Energy Environ Sci* **2015**, *8*, 995–1004. **https://doi.org/10.1039/C4EE03664F**
19. Ocaña, L., Montes, C., González-Díaz, B., González-Pérez, S., Llarena, E. Evaluation of ethylene-vinyl acetate, methyl methacrylate, and polyvinylidene fluoride as encapsulating materials for perovskite-based solar cells using the low-temperature encapsulation method in a cleanroom environment. *Energies* **2024**, *17*, 60. https://doi.org/10.3390/en17010060
20. Emery, Q., Dagault, L., Khenkin, M., Kyranaki, N., Bernardes de Araújo, W. M., Erdil, U., Demuylder, M., Cros, S., Schlatmann, R., Stannowski, B., Ulbrich, C. Tips and tricks for a good encapsulation for perovskite-based solar cells. *Prog Photovolt Res Appl* **2025**, *33*, 551–559. https://doi.org/10.1021/acsami.1c14720